PERGAMON

International Journal of Solids and Structures 39 (2002) 3469–3486

INTERNATIONAL JOURNAL OF SOLIDS and STRUCTURES

www.elsevier.com/locate/ijsolstr

Finite element analysis of localization in FCC polycrystalline sheets under plane stress tension

K. Inal [a], P.D. Wu [b], K.W. Neale [a,*]

[a] *Faculty of Engineering, University of Sherbrooke, Sherbrooke, Que., Canada J1K 2R1*
[b] *Alcan International Limited, Kingston R&D Centre, Kingston, Ont., Canada K7L 5L9*

Received 27 July 2001; received in revised form 27 September 2001

Abstract

Localization phenomena in thin sheets subjected to plane stress tension are investigated. The sheet is modelled as a polycrystalline aggregate, and a finite element analysis based on rate-dependent crystal plasticity is developed to simulate large strain behaviour. Accordingly, each material point in the specimen is considered to be a polycrystalline aggregate consisting of a large number of FCC grains. The Taylor model of crystal plasticity theory is assumed. This analysis accounts for initial textures as well as texture evolution during large plastic deformations. The numerical analysis incorporates certain parallel computing features. Simulations have been carried out for an aluminum sheet alloy, and the effects of various parameters on the formation and prediction of localized deformation (in the form of necking and/or in-plane shear bands) are examined.

Keywords: Polycrystalline sheets; Localized deformations; Necking; In-plane shearing; Numerical simulations

1. Introduction

In the early stages of tensile straining, ductile metals generally exhibit deformation patterns that, on a macroscopic scale, are essentially homogeneous. With continued straining, however, the homogeneous deformation patterns are observed to give way to non-homogeneous modes of deformation, either through the onset of diffuse necking (Hutchinson and Neale, 1977, 1978a, 1978b) and/or localized shearing (Peirce et al., 1982, 1983). Failure usually ensues either by necking down to a "chisel edge", or by rupture within intense shear bands.

It is well known that the localization of plastic flow is strongly influenced by deformation-induced textures and anisotropy (e.g., Asaro and Needleman, 1985). In turn, this localization can then affect, to some degree, the texture development in a polycrystal. This suggests that polycrystal deformation models are required to properly simulate plastic instability and localization phenomena. It is thus expected that polycrystal models can provide an improved understanding of the relation of localization to the microstructure

* Corresponding author. Fax: +1-819-821-7974.
E-mail address: kenneth.neale@courrier.usherb.ca (K.W. Neale).

0020-7683/02/$ - see front matter
PII: S0020-7683(02)00162-2

of the material, and can consequently be more successful in predicting strain localization than can macroscopic, phenomenological models.

There are essentially two main approaches for plastic instability predictions; namely, analyses based on rate-insensitive models of material behaviour and those which assume rate-sensitive response. For a rate-insensitive solid, plastic instability occurs either as a bifurcation state for a perfect specimen, or as an imperfection-triggered localization. For rate-sensitive materials, bifurcation is effectively excluded; however, small inhomogeneites (material and/or geometric) can still result in localization. In the limit of low rate-sensitivity, the localization strain predicted for a given initial inhomogeneity approaches that predicted for the corresponding rate-insensitive solid, while for higher material rate-dependence, localization can be retarded considerably (Hutchinson and Neale, 1977).

For ductile single crystals, the work of Peirce et al. (1982) represents one of the first applications of finite element analysis to model non-uniform modes of deformation. Their analysis, based on a rate-independent constitutive model for crystallographic slip, highlighted inherent limitations of the rate-independent idealization of crystalline slip. As a result of these limitations, Peirce et al. (1983) subsequently developed an analysis based on rate-dependent material response and simulated large strain tension tests for single crystals. Their results provided a general understanding of the roles of rate sensitivity and lattice kinematics in the development of localized modes of deformation under plane strain tension.

Simulations for single crystals are able to provide some insight into the micromechanics of localized deformation phenomena in polycrystalline materials. However, the common metals of industrial practice are polycrystalline aggregates, and there are relatively few finite element analyses for such polycrystals as the solution of the boundary value problems involved can be prohibitive due to the significantly large requirements in computational resources.

In a recent study, Inal et al. (2002) investigated instabilities and localized deformations in polycrystalline solids under plane strain tension. They examined the effects of various parameters on the formation and prediction of localized deformations (in the form of necking and/or shear bands). That work illustrated the importance of texture evolution on the formation of shear bands. In this paper, the non-uniform deformation of thin polycrystalline sheets subjected to plane stress tension are simulated using a polycrystal model-based finite element code. The analysis assumes no initial imperfections, and localized deformation occurs as a result of the imposed boundary conditions at the ends of the specimen. This numerical analysis also incorporates specially developed in-house parallel computing algorithms.

We first recapitulate the constitutive model. Then the finite element formulation is briefly presented. In the last section we present results for an aluminum sheet alloy and discuss the effects of various parameters on the formation of localized deformations. Criteria for the onset of both necking and in-plane shear localization are also introduced.

2. Constitutive model

The polycrystal plasticity model formulated by Asaro and Needleman (1985) and used by Wu et al. (1996) is employed in this analysis. Accordingly, the total deformation of a crystallite is taken to be the result of two distinct physical mechanisms: crystallographic slip due to dislocation motion on the active slip systems, and elastic lattice distortion. Within an FCC crystal, plastic deformation occurs by crystallographic slip on the $12\{1\,1\,1\}\langle 1\,1\,0\rangle$ slip systems where the slip planes are the $\{1\,1\,1\}$ crystallographic planes with normals $\boldsymbol{m}$, and the $\langle 1\,1\,0\rangle$ directions are the shear directions with slip vectors $\boldsymbol{s}$. Plastic deformation is envisaged to occur as a set of plastic simple shears along the various slip systems, leaving the lattice and the slip system vectors $(\boldsymbol{s}_{(\alpha)}, \boldsymbol{m}_{(\alpha)})$ not only essentially undistorted, but also unrotated. (The brackets for the subscripts α indicate that α is not a tensor index and ranges from one to the total number of slip systems.)

Next, the material and lattice are considered to deform elastically and rotate rigidly from the plastically deformed state to the current configuration.

The deformation gradient $\boldsymbol{F}$ is written as

$$\boldsymbol{F} = \boldsymbol{F}^{*}\boldsymbol{F}^{\mathrm{p}}, \tag{1}$$

where $\boldsymbol{F}^{\mathrm{p}}$ consists solely of crystallographic slipping along the specific slip systems, while the elastic deformation and any rigid body rotation is embodied in $\boldsymbol{F}^{*}$. From (1), the spatial gradient of velocity can be written as

$$\boldsymbol{L} = \dot{\boldsymbol{F}}\boldsymbol{F}^{-1} = \boldsymbol{L}^{*} + \boldsymbol{L}^{\mathrm{p}}, \tag{2}$$

where

$$\boldsymbol{L}^{*} = \dot{\boldsymbol{F}}^{*}\boldsymbol{F}^{*^{-1}}, \quad \boldsymbol{L}^{\mathrm{p}} = \boldsymbol{F}^{*}(\dot{\boldsymbol{F}}^{\mathrm{p}}\boldsymbol{F}^{\mathrm{p}^{-1}})\boldsymbol{F}^{*^{-1}}. \tag{3}$$

Taking symmetric and antisymmetric parts of the above relations leads to the elastic and plastic strain-rates $\boldsymbol{D}^{*}$ and $\boldsymbol{D}^{\mathrm{p}}$, the so-called plastic spin $\boldsymbol{W}^{\mathrm{p}}$, and the spin $\boldsymbol{W}^{*}$ associated with the rigid lattice rotation

$$\boldsymbol{D} = \boldsymbol{D}^{*} + \boldsymbol{D}^{\mathrm{p}}, \quad \boldsymbol{W} = \boldsymbol{W}^{*} + \boldsymbol{W}^{\mathrm{p}}. \tag{4}$$

The vectors $\boldsymbol{s}_{(\alpha)}$ and $\boldsymbol{m}_{(\alpha)}$ are regarded as lattice vectors so that they stretch and rotate by

$$\boldsymbol{s}^{*}_{(\alpha)} = \boldsymbol{F}^{*}\boldsymbol{s}_{(\alpha)}, \quad \boldsymbol{m}^{*}_{(\alpha)} = \boldsymbol{m}_{(\alpha)}\boldsymbol{F}^{*-1}. \tag{5}$$

By introducing the following symmetric and skew-symmetric tensors for each slip system α,

$$\boldsymbol{P}_{(\alpha)} = \frac{1}{2}\left[\boldsymbol{s}^{*}_{(\alpha)} \otimes \boldsymbol{m}^{*}_{(\alpha)} + \boldsymbol{m}^{*}_{(\alpha)} \otimes \boldsymbol{s}^{*}_{(\alpha)}\right], \tag{6}$$

$$\boldsymbol{W}_{(\alpha)} = \frac{1}{2}\left[\boldsymbol{s}^{*}_{(\alpha)} \otimes \boldsymbol{m}^{*}_{(\alpha)} - \boldsymbol{m}^{*}_{(\alpha)} \otimes \boldsymbol{s}^{*}_{(\alpha)}\right], \tag{7}$$

the plastic strain-rate and spin for the crystal can be, respectively, written as

$$\boldsymbol{D}^{\mathrm{p}} = \sum_{\alpha} \boldsymbol{P}_{(\alpha)}\dot{\boldsymbol{\gamma}}_{(\alpha)}, \quad \boldsymbol{W}^{\mathrm{p}} = \sum_{\alpha} \boldsymbol{W}_{(\alpha)}\dot{\boldsymbol{\gamma}}_{(\alpha)} \tag{8}$$

where $\dot{\boldsymbol{\gamma}}_{(\alpha)}$ is the shear rate on the slip system α.

The elastic constitutive equation for a crystal is specified by

$$\overset{\triangledown}{\boldsymbol{\tau}}^{*} = \dot{\boldsymbol{\tau}} - \boldsymbol{W}^{*}\boldsymbol{\tau} + \boldsymbol{\tau}\boldsymbol{W}^{*} = \mathscr{L}\boldsymbol{D}^{*}, \tag{9}$$

where $\overset{\triangledown}{\boldsymbol{\tau}}^{*}$ is the Jaumann rate of the Kirchhoff stress tensor $\boldsymbol{\tau}$ based on the lattice rotations, and $\mathscr{L}$ is the tensor of the elastic moduli. These moduli are based on the anisotropic elastic constants of the FCC crystals and thus exhibit the appropriate cubic symmetry.

In order to express the constitutive equation (9) in terms of the Jaumann rate $\overset{\triangledown}{\boldsymbol{\sigma}}$ of the Cauchy stress $\boldsymbol{\sigma} = \det(\boldsymbol{F})^{-1}\boldsymbol{\tau}$, based on the continuum slip $\boldsymbol{W}$, we introduce a second-order tensor $\boldsymbol{R}_{(\alpha)}$ for each slip system as follows:

$$\boldsymbol{R}_{(\alpha)} = \mathscr{L}\boldsymbol{P}_{(\alpha)} + \boldsymbol{W}_{(\alpha)}\boldsymbol{\sigma} - \boldsymbol{\sigma}\boldsymbol{W}_{(\alpha)}. \tag{10}$$

Using (4)–(8) and (10), the constitutive equation (9) can be rewritten in the form

$$\overset{\triangledown}{\boldsymbol{\sigma}} = \mathscr{L}\boldsymbol{D} - \dot{\boldsymbol{\sigma}}^{0} - \boldsymbol{\sigma}\mathrm{tr}\boldsymbol{D}, \tag{11}$$

where $\dot{\boldsymbol{\sigma}}^0$ is a viscoplastic type stress-rate defined by

$$\dot{\boldsymbol{\sigma}}^0 = \sum_{\alpha} \boldsymbol{R}_{(\alpha)} \dot{\gamma}_{(\alpha)}. \tag{12}$$

The slip rates to be substituted into Eq. (12) are assumed to be governed by the following power-law expression:

$$\dot{\gamma}_{(\alpha)} = \dot{\gamma}_{(0)} \operatorname{sgn} \tau_{(\alpha)} \left| \frac{\tau_{(\alpha)}}{g_{(\alpha)}} \right|^{1/m}. \tag{13}$$

Here $\dot{\gamma}(0)$ is a reference shear rate taken to be the same for all the slip systems, $\tau_{(\alpha)} = \boldsymbol{P}_{(\alpha)} : \boldsymbol{\sigma}$ is the resolved shear stress on slip system α, $g_{(\alpha)}$ is its hardness and m is the strain-rate sensitivity index. The functions $g_{(\alpha)}$ characterize the current strain-hardened state of all slip systems. The rate of increase of the function $\dot{g}_{(\alpha)}$ is defined by the hardening law:

$$\dot{g}_{(\alpha)} = \sum_{\beta} h_{(\alpha\beta)} \left| \dot{\gamma}_{(\beta)} \right|, \tag{14}$$

where $g_{(\alpha)}(0)$ is the initial hardness, taken to be a constant τ_0 for each slip system, and $h_{(\alpha\beta)}$ are the hardening moduli. The form of these moduli is

$$h_{(\alpha\beta)} = q_{(\alpha\beta)} h_{(\beta)} \quad (\text{no sum on } \beta) \tag{15}$$

where $h_{(\beta)}$ is a single slip hardening rate, and $q_{(\alpha\beta)}$ is the matrix describing the latent hardening behaviour of the crystallite.

Asaro and Needleman (1985), among others, simply take each $g_{(\alpha)}$ to depend on the accumulated sum γ_{a} of the slips; i.e.,

$$g_{(\alpha)} = g_{(\alpha)}(\gamma_{\mathrm{a}}), \quad \gamma_{\mathrm{a}} = \int_0^t \sum_{\alpha} |\dot{\gamma}_{(\alpha)}| \, \mathrm{d}t. \tag{16}$$

Based on measurements of strain hardening of single crystals of aluminum alloys by Chang and Asaro (1981), the following slip hardening rate was used by Asaro and co-workers:

$$h_{\beta} = h_{\mathrm{s}} + (h_0 - h_{\mathrm{s}}) \operatorname{sech}^2 \left\{ \left(\frac{h_0 - h_{\mathrm{s}}}{\tau_{\mathrm{s}} - \tau_0} \right) \gamma_{\mathrm{a}} \right\}, \tag{17}$$

where h_0 and h_{s} are the system's initial and asymptotic hardening rates. If $h_{\mathrm{s}} = 0$, then τ_{s} represents the saturation value of the shear stress.

The response of a polycrystal comprised of many grains is obtained by invoking the Taylor assumption. Thus, at a material point representing a polycrystal of N grains, the deformation in each grain is taken to be identical to the macroscopic deformation of the continuum. Furthermore, the macroscopic values of all quantities, such as stresses, stress-rates and elastic moduli, are obtained by averaging their respective values over the total number of grains at the particular material point.

3. Finite element implementation

A finite element procedure based on a Lagrangian formulation of the field equations has been developed. Thus if $\boldsymbol{g}_i$ are the base vectors in the undeformed configuration corresponding to the convected coordinates x_i, the deformed base vectors are $\boldsymbol{G}_i = \boldsymbol{F}\boldsymbol{g}_i$. The initial, undeformed configuration of the body with volume

V and surface S is used as a reference. Then, for quasi-static deformations and in the absence of body forces, the equilibrium equations are expressed through the virtual work condition

$$\int_V \tau^{ij}\,\delta\eta_{ij}\,\mathrm{d}V = \int_S T^i\,\delta u_i\,\mathrm{d}S \tag{18}$$

for arbitrary variations of the displacement components u_i and corresponding variations of the components η_{ij} of the Lagrangian strain tensor. Here, τ^{ij} are the components on the undeformed basis of the second Piola–Kirchhoff tensor and T^i are the corresponding traction vectors.

In the linear incremental problem, we suppose the current state of approximate equilibrium to be known at time t. To determine the equations for the field quantity rates, Eq. (18) is expanded in a Taylor series about the time t to yield (Needleman and Tvergaard, 1984)

$$\Delta t \int_V \left(\dot{\tau}^{ij}\,\delta\eta_{ij} + \tau^{ij}\dot{u}^k_{,i}\,\delta u_{k,j}\right)\mathrm{d}V = \Delta t \int_S \dot{T}^i\,\delta u_i\,\mathrm{d}S - \left[\int_V \tau^{ij}\,\delta\eta_{ij}\,\mathrm{d}V - \int_S T^i\,\delta u_i\,\mathrm{d}S\right]. \tag{19}$$

The last term on the right-hand side of (19) serves as an equilibrium correction if equilibrium in the current state is only approximate.

3.1. Problem formulation

A thin, orthotropic sheet specimen submitted to uniaxial tension along the x_1-axis is modelled (Fig. 1) under the assumption of plane stress conditions in the plane of the sheet. The analysis assumes no initial geometric imperfection. The specimen is assumed to be clamped at the ends ($x_1 = \pm L_0$) and the resulting inhomogeneous behaviour is what eventually initiates localized deformation modes. Simulations are performed for specimens rotated such that the rolling direction of the sheet is oriented at 0°, 1°, 45° and 90° with respect to the axis of tensile loading.

As a result of orthotropy it can be assumed that $D_{13} = D_{23} = W_{13} = W_{23} = 0$, where W_{13} and W_{23} are the components of the skew-symmetric spin tensor. The strain-rate component D_{33} is determined from the condition that the average stress component $\dot{\sigma}_{33} = 0$. For the orthotropic texture considered, these conditions imply that the average stress components $\sigma_{13} = \sigma_{23} = 0$.

When x_1 and x_2 are assumed to coincide with the rolling and transverse directions of the sheet, respectively, the behaviour can be considered to be symmetric about the central lines $x_1 = 0$ and $x_2 = 0$. In such cases (e.g., for the 0° and 90° oriented specimens) only one-quarter of the specimen is considered in the numerical solutions, as shown in Fig. 1. In view of the symmetry and the assumption that the specimen is clamped at the ends, the boundary conditions on the quadrant are as follows:

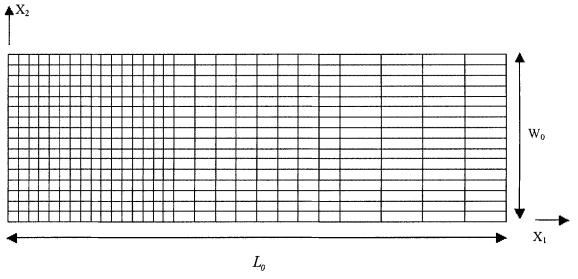

Fig. 1. Finite element mesh used in 0° and 90° rotated specimen simulations.

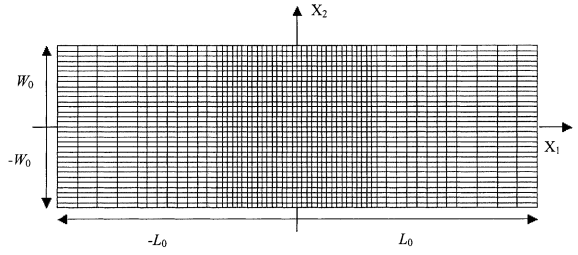

Fig. 2. Finite element mesh used in 1° and 45° rotated specimens.

$$\begin{aligned} &u_2 = 0 \text{ along } x_2 = 0,\\ &u_1 = 0 \text{ along } x_1 = 0,\\ &u_2 = 0 \text{ along } x_1 = L_0,\\ &\dot{u}_1 = V \text{ (applied velocity) along } x_1 = L_0. \end{aligned} \tag{20}$$

Thus, the end of the specimen $x_1 = L_0$ is not shear free. Also, note that thinning (deformation through the thickness of the sheet) is permitted at the ends of the specimen.

Specimens where the RD is oriented at 1° and 45° with respect to the tensile axis are also considered. For these cases the assumption of symmetric behaviour with respect to the reference axes is obviously no longer valid, and the entire specimen has to be modelled in the numerical analysis. The finite element mesh used to model the entire specimen is shown in Fig. 2. The boundary conditions for simulations with the full mesh are:

$$\begin{aligned} &u_2 = 0 \text{ along } x_1 = \pm L_0,\\ &\dot{u}_1 = V \text{ (applied velocity) along } x_1 = L_0,\\ &\dot{u}_1 = -V \text{ (applied velocity) along } x_1 = -L_0. \end{aligned} \tag{21}$$

Again, the ends of the specimen, $x_1 = \pm L_0$, are not shear free.

The finite element model incorporates certain parallel computing algorithms so that simulations could be performed with models containing sufficiently large numbers of elements. The parallel algorithms used in our simulations are designed to distribute data on the microscopic level (crystal data) over the processors of an IBM SP3 supercomputer. Details regarding the parallelization features of the numerical analysis can be found in Inal et al. (2000, 2002).

4. Results and discussion

The texture considered corresponds to a commercial aluminum sheet alloy (AA3004-H19) and is represented by 380 discrete orientations in Euler space. Fig. 3 shows the {1 1 1} pole figure based on the texture characterization provided by the manufacturer where this representation with 380 grains was considered to be sufficient to capture the components of a typical rolling texture and to assure orthotropic material symmetry. Here again, X_1 and X_2 refer to the rolling and the transverse directions of the sheet, respectively. The values of the material properties used in the simulations are

$$\tau_0 = 95 \text{ MPa}, \quad h_0/\tau_0 = 1.2, \quad \tau_s/\tau_0 = 1.16, \quad h_s/\tau_0 = 0, \quad q = 1.0. \tag{22}$$

These properties were obtained by fitting the uniaxial stress–strain curve obtained by the polycrystal plasticity model (assuming homogeneous plane stress tension in the RD) to the uniaxial stress–strain curve

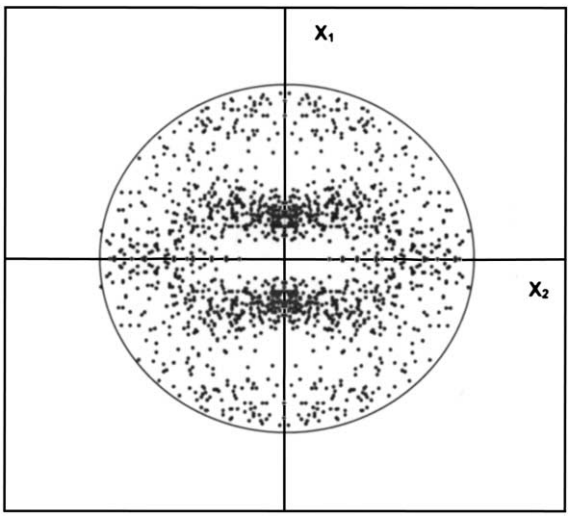

Fig. 3. Initial texture of AA3004-H19 represented by {1 1 1} stereographic pole figure.

measured experimentally (Inal et al., 2000). The slip system reference plastic shearing rate $\dot{\gamma}_0$ and the slip rate sensitivity parameter m are taken as $\dot{\gamma}_0 = 0.001\ s^{-1}$, and $m = 0.002$, respectively, with the crystal elastic constants taken as $C_{11} = 206$, $C_{12} = 118$ and $C_{44} = 54$ GPa. The initial geometry of the specimen is such that $L_0/W_0 = 3$, and this value is used for all simulations presented in this work unless indicated otherwise.

4.1. A typical result

A comparison between the experimental true stress–true strain curve for uniaxial tension in the RD with that obtained from the finite element simulation for the polycrystal is presented in Fig. 4. It can be seen that the FE simulation is in very good agreement with the experimental curve. The failure strain has been over-predicted by our simulation, but this is perhaps due to the fact that the simulation is carried out without

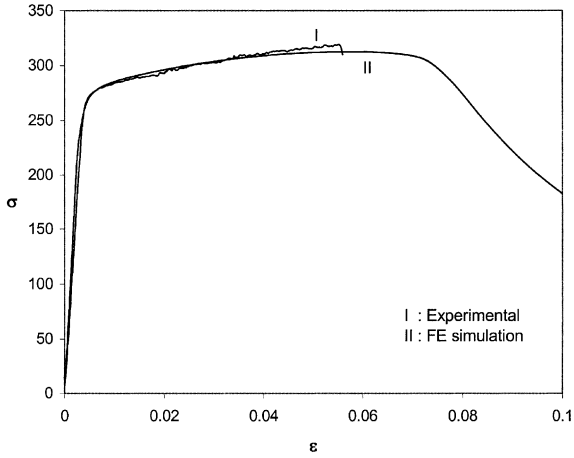

Fig. 4. True stress–strain curves in RD.

any initial geometric imperfection. In addition, the crystal plasticity model employed in this study does not account for microscopic defects, such as voids, which will undoubtedly influence the failure strain.

4.2. Mesh sensitivity

Localized shearing phenomena are notorious for sometimes exhibiting a pathological mesh sensitivity in finite element simulations. However, as demonstrated by Needleman (1988), this is not necessarily the case for our type of simulations where the inherent mesh sensitivity associated with a rate-independent theory can be mitigated by using a rate-dependent material formulation such as the one used in this study. Nevertheless, the selection of a proper mesh does require attention. Fig. 5 illustrates the three different finite element meshes used in this study with 288, 448 and 864 elements, respectively.

The numerical studies show that the overall stress–strain curves for all three meshes are nearly identical in terms of strain hardening and saturation (Fig. 6). However, once softening occurs, the finer meshes demonstrate stronger softening effects. Fig. 7a–c illustrate the contours of true strain (in the loading direction) at an elongation of $U/L_0 = 0.10$ for the three meshes considered. These simulations show that the initiation and propagation of in-plane shear bands are not sensitive to the meshes considered; for all cases, localized deformation in the form of two shear bands intersecting at the centre of the specimen are formed. It is also observed that, the finer is the mesh, the narrower and stronger are the shear bands, although this does not have a significant impact on the general features of localized deformation.

The mesh sensitivity analysis presented above was performed by keeping the element aspect ratio constant. Recently, Inal et al. (2002) presented a mesh sensitivity analysis where they considered different element aspect ratios to investigate localized deformation in an aluminum sheet alloy under plane strain

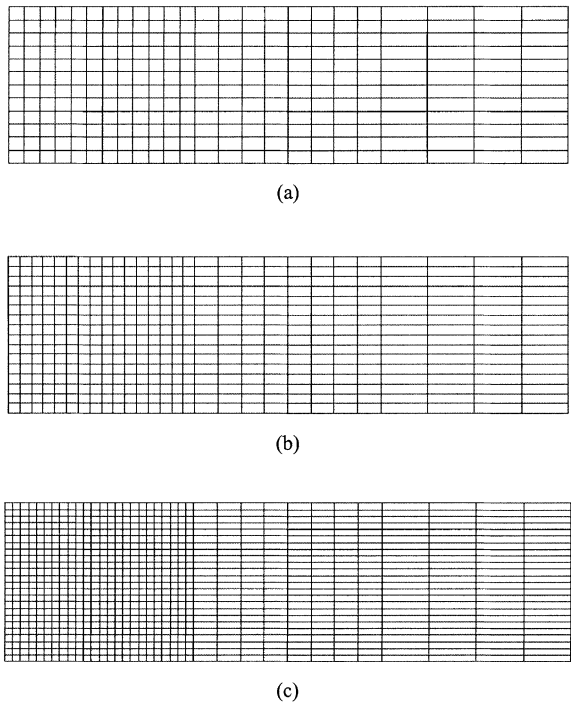

Fig. 5. Initial meshes used in the mesh sensitivity analysis: (a) 288, (b) 448 and (c) 864 elements.

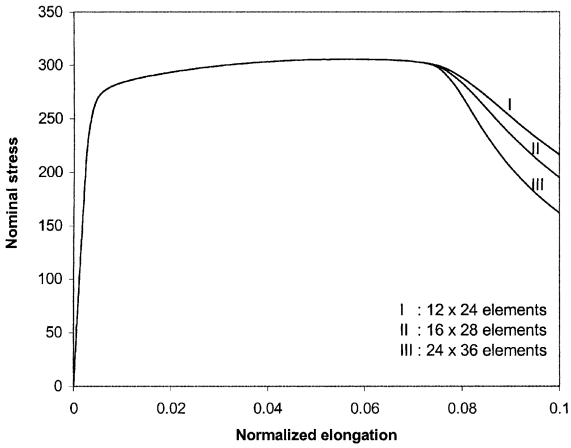

Fig. 6. Nominal stress–normalized elongation curves for three different meshes.

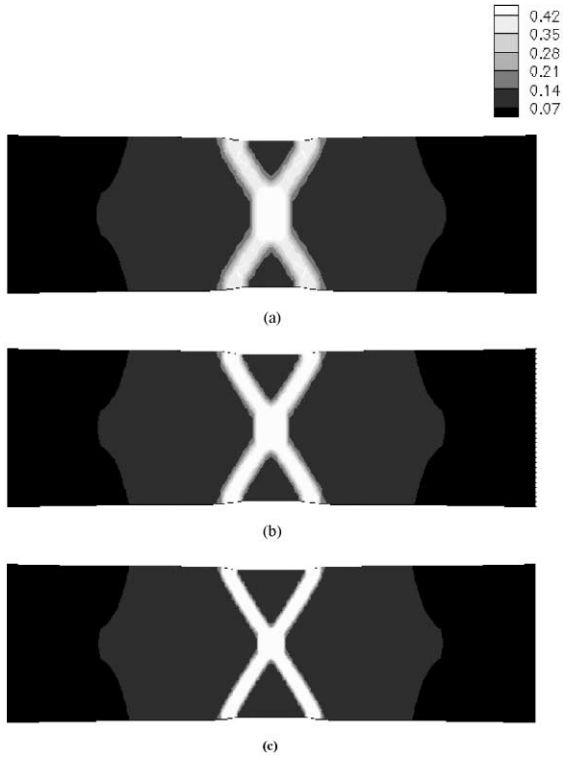

Fig. 7. Contour plots of true strain (in loading direction) at $U/L_0 = 0.1$ for: (a) 12×24, (b) 16×28 and (c) 24×36 elements.

tension. That study showed that the element aspect ratio can indeed affect the predictions of localization. Based on the mesh sensitivity analysis performed in this paper, and the results of the mesh sensitivity analysis presented by Inal et al. (2002), it was concluded that the relatively fine mesh (16×28) with an

element aspect ratio of 1 was sufficiently accurate to capture the key features of localized deformation. This mesh was therefore used for all simulations with one-quarter of the specimen, while a mesh of 32×56 elements was employed for the simulations of the complete specimen.

4.3. Uniaxial tension along the RD, at 45° from the RD, and along the TD

We now present results for uniaxial tension simulations along the RD, for tension at 45° to the RD, and for tension along the TD. Henceforth, these will be referred to as the RD, 45° and TD simulations, respectively. The nominal stress–strain curves for the RD, 45° and TD simulations are compared in Fig. 8. These simulations show that the nominal stress–normalized elongation curves for the RD and 45° simulations are quite similar, while the TD simulation results in a somewhat higher curve. The maximum nominal stresses are obtained at $U/L_0 = 0.55$, $U/L_0 = 0.53$ and $U/L_0 = 0.52$ for the RD, 45° and TD simulations, respectively. After saturation, softening occurs for all three orientations, with the 45° simulation exhibiting slightly stronger softening than the other two.

As already mentioned, the RD and TD simulations are carried out by modelling one-quarter of the specimen with the assumption of orthotropic symmetry. Since that assumption is not valid for the 45° simulations, the full specimen was modelled for this case. In order to analyse the sensitivity of the results to the loading direction, we have compared uniaxial tension along the RD with a very slightly rotated specimen having the RD oriented at 1° with respect to the axis of loading. The complete specimen has been modelled for both these cases. For the RD simulations, as expected (due to orthotropic symmetry), two

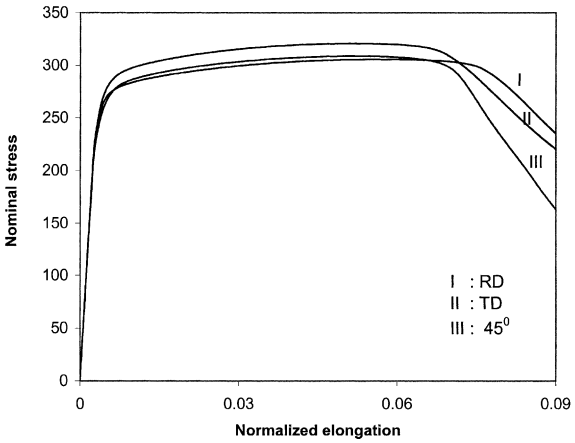

Fig. 8. Nominal stress–strain curves for uniaxial tension along the RD, 45° from the RD and TD.

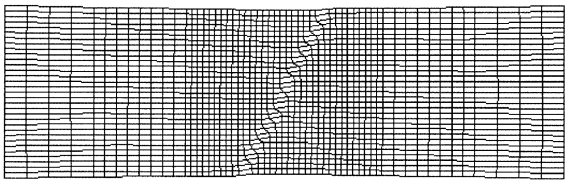

Fig. 9. Deformed mesh for 1° simulation at $U/L_0 = 0.09$.

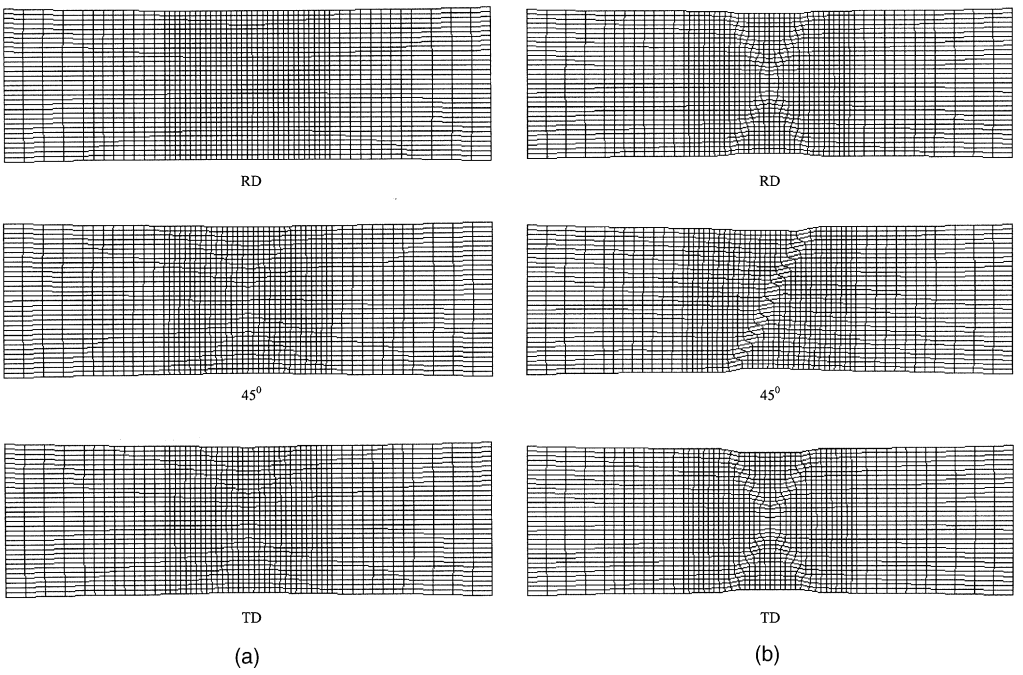

Fig. 10. Deformed meshes for the RD, 45° and TD simulations at: (a) $U/L_0 = 0.07$ and (b) $U/L_0 = 0.09$.

shear bands are predicted, similar to what was presented in Fig. 7b. However, when the specimen is rotated even as slightly as 1° to the tensile axis, only one shear band is predicted, as seen in Fig. 9.

Results for the deformed meshes of the RD, 45° and TD simulations are presented in Fig. 10. Fig. 10a shows the deformed meshes at $U/L_0 = 0.07$ (after the maximum nominal stresses for all three orientations), where very slight diffused necks have formed for all three orientations. Shear bands are fully developed for all three orientations at $U/L_0 = 0.09$ (Fig. 10b). Here the RD and TD simulations indicate two shear bands intersecting at the centre of the specimen, while the 45° simulation predicts only one shear band.

A more quantitative representation of in-plane shear band development is presented in Fig. 11a and b, where contours of true strain (in the loading direction) are plotted at various stages of deformation. Fig. 11a corresponds to Fig. 10a, where $U/L_0 = 0.07$. The strain distribution is observed to be non-uniform for all orientations indicating localized deformation. For the RD simulation, the concentration of strain at the centre of the specimen indicates early stages of necking; however, there are no signs of shear localization. By contrast, for the TD and 45° simulations shear band patterns are evident with two bands for the TD simulation and a single band for the 45° simulation as indicated by the 0.21 strain contours. With further straining, it can be seen that shear bands also develop with the RD simulation. The strain in the shear bands exceed 0.35 although the overall normalized extension is $U/L_0 = 0.09$ (Fig. 11b). Thus, while there is very little deformation occurring outside the shear bands, a large amount of shear is accumulating within these well-defined shear bands.

4.4. Onset of localization for 45° simulation

As has already been discussed, numerous analytical and numerical investigations have been carried out to investigate the onset of necking and in-plane shear localization. In this section we will investigate both the onset of necking and shear banding for the 45° simulations.

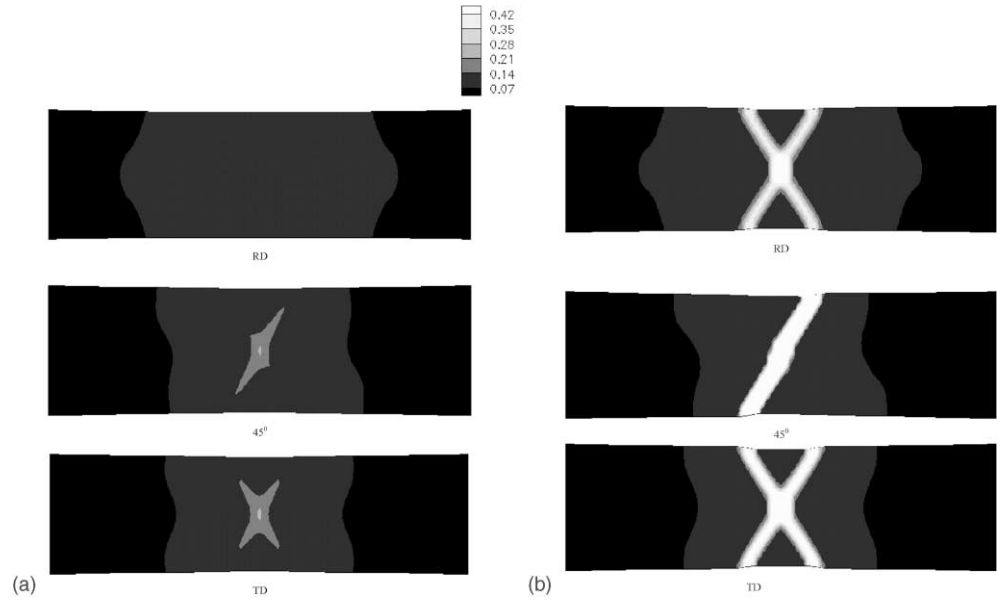

Fig. 11. Contours of true strain (in loading direction) for the RD, 45° and TD simulations at: (a) $U/L_0 = 0.07$ and (b) $U/L_0 = 0.09$.

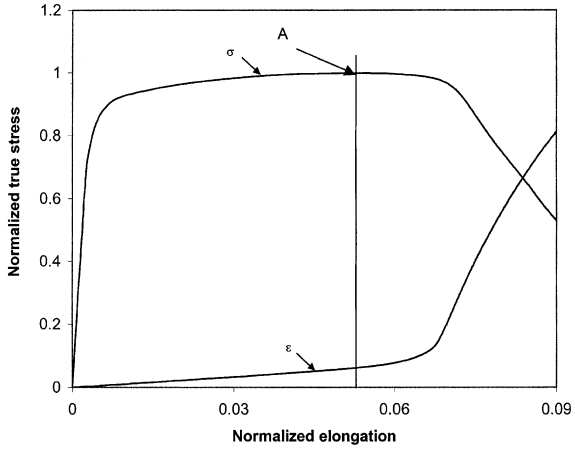

Fig. 12. The evolution of the true strain ε (averaged at the centre of the specimen) and the true stress σ (averaged at the end of the specimen).

In Fig. 12 the normalized stress $\sigma/\sigma_{\max}$ is plotted as a function of the normalized elongation. Here, $\sigma_{\max}$ refers to the maximum value of the physical component of the true stress (in the loading direction) calculated at the end section of the specimen, $x_1 = L_0$. It can be seen that σ reaches a maximum around $U/L_0 = 0.052$ (point A), and then begins to decrease. The evolution of the true strain ε (in the loading direction) measured at the centre of the specimen is also included in Fig. 12. The results show that the attainment of the maximum stress at $U/L_0 = 0.052$ (point A) is associated with the onset of diffuse necking; beyond this elongation the strain ε begins to increase rapidly, thus signifying localization.

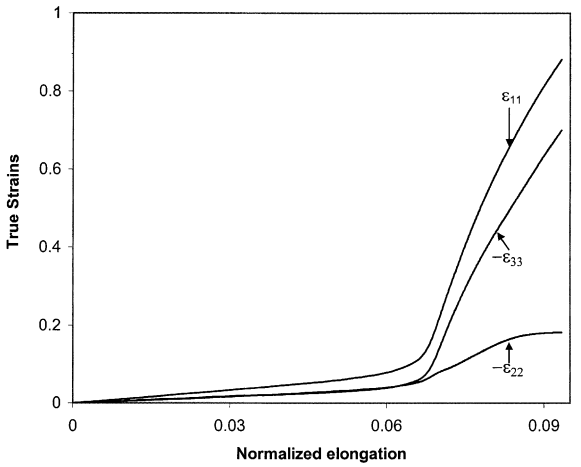

Fig. 13. The evolution of the true strains ε_{ii} at the centre of the specimen.

It should be mentioned that the nominal stress (calculated at the end section of the specimen) for the 45° simulation also reaches a maximum around $U/L_0 = 0.052$. This is because of the relatively low strain-rate sensitivity ($m = 0.002$) used in the analysis. When the strain-rate sensitivity is increased, there is a significant difference between the elongations that the nominal and true stresses reach their maximum values, as was demonstrated by Inal et al. (2002), where m was taken as 0.02. For cases with high strain-rate sensitivity, the elongation value where the true stress σ reaches a maximum is taken as the value for the onset of diffuse necking.

The evolution of the true strain components measured at the centre of the specimen are presented in Fig. 13. Here we observe that the deformations are almost uniform up to the onset of necking (which corresponds to the attainment of the maximum true stress at the end of the specimen). With continued stretching, sharp changes in the strains at the neck section occur, thus signifying localization. A comparison of Fig. 10(b) with Fig. 13 shows that in-plane shear localization is accompanied by significant localized thinning. Note that while ε_{11} and $-\varepsilon_{33}$ increase at approximately similar rates, $-\varepsilon_{22}$ reaches a maximum value at an elongation of $U/L_0 = 0.088$, and then remains nearly constant at this value during further deformation. Thus, the deformation at the centre of the specimen approaches in-plane plane strain.

Although an appropriate approximate criterion for the onset of diffuse necking has been known for some time, quantitative criteria for the initiation of localized shearing are more recent in origin. Initially, localized shearing was associated with reaching an ideally plastic state. In fact, for crystals undergoing single slip and obeying the Schmid criterion for continued yielding, it is necessary for the slip plane work hardening rate to vanish in order for localized shearing to initiate. However, in most cases shear band formation is observed in crystals undergoing multi-slip, often with a double mode of primary-conjugate slip. Employing a planar idealization of this primary-conjugate slip mode Asaro (1979) found that, for single crystals, shear band initiation is associated with the attainment of a critically small positive value of the ratio of slip plane hardening rate to the current stress level.

In this study, a macroscopic parameter is introduced to define a criterion for the onset of in-plane shear banding. The onset of diffuse necking (Fig. 12) has already been associated with the attainment of the maximum true stress *at the end* of the specimen. To determine a criterion for the onset of in-plane shear banding, the true stress–strain curve obtained at the centre of the specimen, averaged along line B–B′ as shown in Fig. 14, is examined. (This average is computed using the values of the true stresses calculated at the integration points of the elements.) If the localization mode is only necking, the stress–strain curve obtained along line B–B′ will always exhibit strain hardening. However, the average true stress calculated

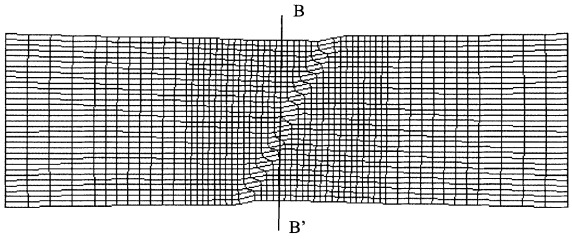

Fig. 14. Deformed mesh for 45° simulation.

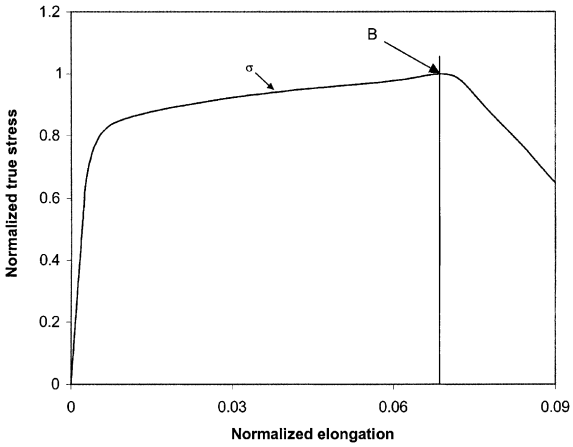

Fig. 15. The evolution of the true stress σ (averaged along line B–B′).

along line B–B′ reaches a maximum around $U/L_0 = 0.068$ (although necking localization is well underway before $U/L_0 = 0.068$); this is identified as point B in Fig. 15. This indicates a change in the localization mode from necking to in-plane shear banding. In order to investigate the localization mode, contour plots of true strain in loading direction at points A (defined in Fig. 12) and B (defined in Fig. 15) are presented in Fig. 16. Fig. 16a corresponds to point A where $U/L_0 = 0.052$. It can be seen that the strain is concentrating towards the centre of the specimen, thus indicating the initial phases of necking. When Fig. 16b (which corresponds to point B where $U/L_0 = 0.068$) is examined, it can be seen that the strain has begun to localize in the form of a band (represented by the 0.12 strain contour), indicating the initiation of in-plane shear banding. Thus, the attainment of the maximum true stress along line B–B′ (at the centre of the specimen) can be taken as an appropriate criterion for the onset of in-plane shear banding. However, the application of this onsetting criterion during laboratory experiments would undoubtedly be very difficult since after the maximum is attained the load drops very abruptly. By the time the drop is noticed, failure might already have already occurred.

4.5. The effect of the specimen aspect ratio

To investigate the effect of the specimen aspect ratio L_0/W_0 on the formation of localized deformation bands, uniaxial tension simulations for specimens oriented at 1° to the tensile axis have been performed where aspect ratios of 2, 3 and 4 were considered. Note that the same numbers of elements were used to model the necking area (Fig. 17) for the three simulations considered.

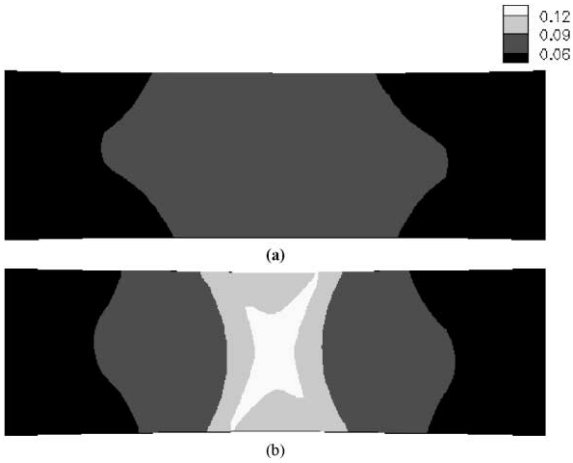

Fig. 16. Contours of true strain (in loading direction) for 45° simulation at: (a) $U/L_0 = 0.052$ and (b) $U/L_0 = 0.068$.

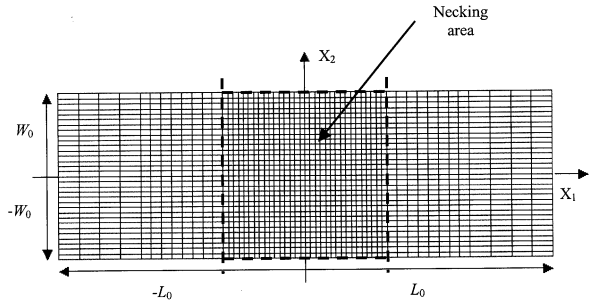

Fig. 17. The necking area considered in the simulations with different specimen aspect ratios.

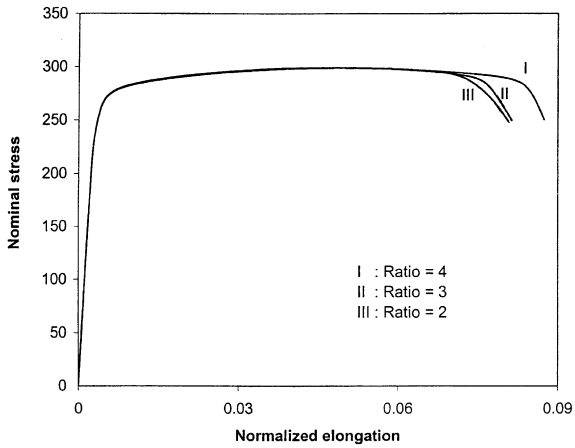

Fig. 18. Nominal stress–normalized elongation curves for simulations with different specimen aspect ratios.

The nominal stress–normalized elongation curves for the different specimen aspect ratios are compared in Fig. 18. These results show that increasing the specimen aspect ratio delays the formation of localized deformation. The delay in the formation of localized deformation bands can be better observed when Fig. 19a–c are examined. A shear band has already initiated in the specimen with the aspect ratio 2 at an elongation of $U/L_0 = 0.07$ (Fig. 19a), while the deformations are more or less homogeneous in the remaining specimens. With further stretching, shear bands are observed in the specimens with the aspect ratios 2 and 3 at an elongation of $U/L_0 = 0.08$ (Fig. 19b). For the specimen with the highest aspect ratio, a shear band develops at an elongation of $U/L_0 = 0.08$ (Fig. 19c).

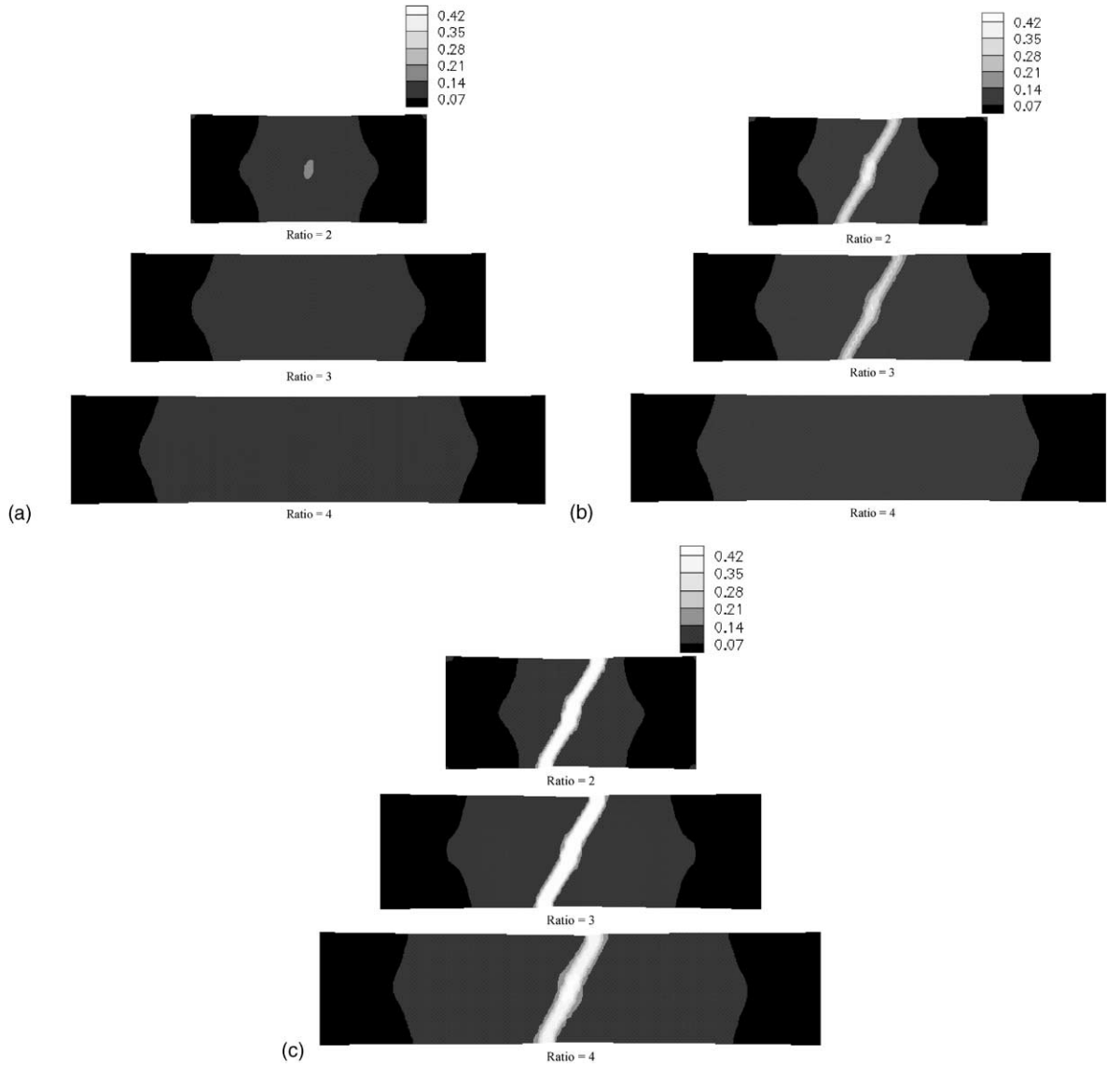

Fig. 19. Contour plots of true strain (in loading direction) for specimens with different aspect ratios at: (a) $U/L_0 = 0.07$, (b) $U/L_0 = 0.08$ and (c) $U/L_0 = 0.09$.

5. Conclusion

A plane stress crystal plasticity-based finite element model has been developed to simulate instabilities and localized deformations in polycrystalline solids. The response of a commercial thin sheet aluminum alloy (AA3004-H19) was investigated under conditions of in-plane tension. The initial texture of the polycrystalline sheet was represented by 380 grains. As experimental investigations of very thin sheets typically used in can forming can be difficult due to the limited ductility of these materials, the type of numerical capability developed here can represent a useful tool for the assessment of the effects of various material parameters (e.g., textures) on sheet formability.

Our simulations have shown that the initiation of a neck leads to the formation of localized deformations. For the rate-dependent analysis considered, the onset of necking is associated with the attainment of the maximum stress at the end section of the specimen, away from the neck. For the limiting case of a rate-independent material, this criterion reduces to the attainment of a maximum strain (which is the onset of the elastic unloading) since for the rate-independent analysis the attainment of maximum strain will also correspond to the attainment of the maximum stress.

Once necking has initiated, it triggers the development of in-plane shear localization. Our calculations have shown that it is possible to define an appropriate approximate criterion for the onset of shear localization. The attainment of the maximum stress at the centre of the specimen (calculated as an average over line B–B′ as shown in Fig. 14) corresponded to the onset of shear localization for all three orientations considered in this study. When the localization mode is simply necking without shear banding, the stress calculated at the centre of the specimen does not pass through a maximum since there will always be strain hardening at the centre of the specimen.

A significant mesh sensitivity was not observed for the overall stress response, nor for the general trends for the initiation and propagation of the localized deformation. Our simulations showed that the finer is the mesh, the narrower and sharper become the shear bands. It is important to mention that the mesh sensitivity analysis carried out in this investigation was performed by refining the mesh without modifying the initial element aspect ratio.

One of the factors affecting localized deformation phenomena is the loading direction, since the overall stress response and deformation pattern is sensitive to this. Even the slightest rotation of the loading direction with respect to the rolling direction of the sheet was seen to have a significant effect on the deformation pattern; two shear bands were predicted for uniaxial tension along the RD, while only one single shear band was predicted for uniaxial tension at 1° from the RD.

Another important factor in the formation of localized deformation is the specimen aspect ratio. For the boundary conditions considered, increasing the specimen aspect ratio delayed the formation of localized deformation. However, the specimen aspect ratio did not affect the localized deformation pattern; for all cases considered a single shear band was predicted at approximately 80° to the loading direction.

Finally, it should be emphasized that, since we assume plane stress conditions, through-thickness shear banding is obviously excluded. A full three-dimensional finite element analysis would perhaps provide interesting results regarding the combined interactions of in-plane shear localization, necking, and through-thickness shear banding.

Acknowledgements

This work was supported by the Natural Sciences and Engineering Research Council of Canada (NSERC) and a grant from Alcan International Limited (Kingston Research and Development Centre).

References

Asaro, R.J., Needleman, A., 1985. Texture development and strain hardening in rate dependent polycrystals. Acta Metallurgica 33, 923–953.

Asaro, R.J., 1979. Geometrical effects in the homogeneous deformation of ductile single crystals. Acta Metallurgica 27, 445–453.

Chang, Y.W, Asaro, R.J., 1981. An experimental study of shear localization in aluminum–copper single crystals. Acta Metallurgica 29, 241–254.

Hutchinson, J.W., Neale, K.W., 1977. Influence of strain-rate sensitivity on necking under uniaxial tension. Acta Metallurgica 25, 839–846.

Hutchinson, J.W., Neale, K.W., 1978a. Sheet Necking II. Time-independent behaviour. In: Koistinen, D.P., Wang, N.M. (Eds.), Mechanics of Sheet Metal Forming. Plenum Press, New York, pp. 127–153.

Hutchinson, J.W., Neale, K.W., 1978b. Sheet Necking III. Strain-rate effects. In: Koistinen, D.P., Wang, N.M. (Eds.), Mechanics of Sheet Metal Forming. Plenum Press, New York, pp. 269–285.

Inal, K., Wu, P.D., Neale, K.W., MacEwen, S.R., 2000. Numerical simulation of large deformation polycrystalline plasticity. In: Martin, P., MacEwen, S.R., Verreman, Y., Liu, W., Goldak, J. (Eds.), Mathematical Modelling in Metal Processing and Manufacturing COM2000, Ottawa.

Inal, K., Wu, P.D., Neale, K.W., 2002. Instability and localized deformation in polycrystalline solids under plane strain tension. International Journal of Solids and Structures 39, 983–1002.

Needleman, A., Tvergaard, V., 1984. Finite element analysis of localization in plasticity. In: Oden, J.T., Carey, G.F. (Eds.), Finite Elements Special Problems in Solid Mechanics. Prentice-Hall, Englewood Cliffs, NJ, pp. 94–157.

Needleman, A., 1988. Material rate dependence and mesh sensitivity in localization problems. Computer Methods in Applied Mechanics and Engineering 67, 69–85.

Peirce, D., Asaro, R.J., Needleman, A., 1982. An analysis of nonuniform and localized deformation in ductile single crystals. Acta Metallurgica 30, 1087–1119.

Peirce, D., Asaro, R.J., Needleman, A., 1983. Material rate dependence and localized deformation in crystalline solids. Acta Metallurgica 31, 1951–1976.

Wu, P.D., Neale, K.W., Van der Giessen, E., 1996. Simulation of the behaviour of FCC polycrystals during reversed torsion. International Journal of Plasticity 12, 1199–1219.